We are IntechOpen,
the world's leading publisher of
Open Access books
Built by scientists, for scientists

4,800
Open access books available

122,000
International authors and editors

135M
Downloads

154
Countries delivered to

Our authors are among the

TOP 1%
most cited scientists

12.2%
Contributors from top 500 universities

CLARIVATE ANALYTICS

BOOK CITATION INDEX

INDEXED

WEB OF SCIENCE™

Selection of our books indexed in the Book Citation Index
in Web of Science™ Core Collection (BKCI)

Interested in publishing with us?
Contact book.department@intechopen.com

Numbers displayed above are based on latest data collected.
For more information visit www.intechopen.com

High-Power RF Uni-Traveling-Carrier Photodiodes (UTC-PDs) and Their Applications

Tadao Nagatsuma[1] and Hiroshi Ito[2]
[1]Osaka University,
[2]Kitasato University
Japan

1. Introduction

Research on exploring millimeter waves and/or terahertz (THz) waves, which cover the frequency range from 30 GHz to 10 THz, has lately increased since the nature of these electromagnetic waves is suited to spectroscopic sensing as well as to ultra-broadband wireless communications. One of the obstacles to developing applications of millimeter waves and terahertz waves is a lack of solid-state signal sources.

For the generation of millimeter waves and terahertz waves, photonic techniques are considered to be superior to conventional techniques based on electronic devices with respect to wide frequency bandwidth, tunability, and stability. Moreover, the use of optical fiber cables enables us to distribute high-frequency RF signals over long distances. In this scheme, optical-to-electrical (O-E) converters, or **"photodiodes"**, which operate at long optical wavelengths (1.3-1.55 μm), play a key role, and high output current is required in addition to large bandwidth for practical applications.

Among various types of long-wavelength photodiode technologies, a **uni-traveling-carrier photodiode (UTC-PD) and its derivatives** have exhibited the highest output powers at frequencies from 100 GHz to 1 THz, with improvement in layer and device structures since its debut in 1997 (Ishibashi et al., 1997).

This paper describes recent progress in the high-power RF UTC-PDs, which operate at millimeter-wave and terahertz-wave frequencies. In Section 2, we discuss how its operation mode differs from that of the conventional photodiode. Next, some typical characteristics of the UTC-PD, such as output RF powers and their frequency characteristics, as well as some techniques for enhancing the output powers from the UTC-PD, such as resonant design, antenna integration, and packaging, are presented. In Section 3 we show recent analog applications of the UTC-PD such as wireless communications, spectroscopy, and imaging, which have not been realized with conventional electronics or photodiode technologies.

2. Uni-traveling-carrier photodiode (UTC-PD)

2.1 Concept and operations

Uni-traveling-carrier photodiode (UTC-PD) (Ishibashi et al., 1997, Ito et al., 2004a, 2008) is a novel photodiode that utilizes only electrons as active carriers. This feature is the key for realizing its superior performance. Band diagram of the UTC-PD is shown in Fig. 1(a)

together with that of conventional pin-PD in Fig. 1(b). The active part of the UTC-PD consists of a p-type doped InGaAs light absorption layer and an undoped (or a lightly n-type doped) InP carrier-collection layer. In the UTC-PD, the photo-generated minority electrons in the neutral absorption layer diffuse into the depleted collection layer and then drift to the cathode layer. On the other hand, because the absorption layer is quasi-neutral, photo-generated majority holes respond very fast within the dielectric relaxation time by their collective motion. Therefore, the photoresponse of a UTC-PD is determined only by the electron transport. This is an essential difference from the conventional pin-PD (Fig. 1(b)), in which both electrons and holes contribute to the device response and the low-velocity hole-transport determines the total performance (Furuta et al., 2000). This qualitatively different operation mode of the UTC-PD provides three important advantages.
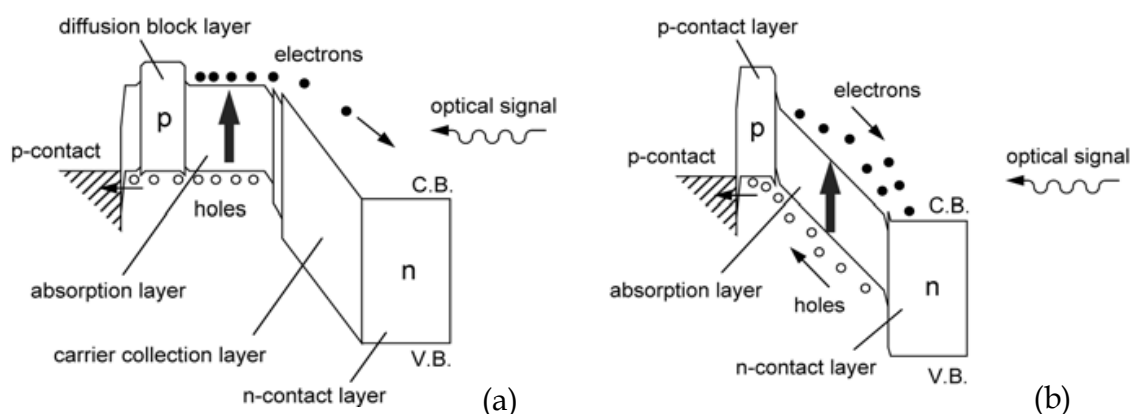

Fig. 1. Band diagram of a UTC-PD (a) and a pin-PD (b).

One is higher operation speed due to an order of magnitude higher electron velocity (Ishibashi et al., 1994) in the depletion layer compared to hole velocity (Hill et al., 1987). Here, we are also benefitted from the velocity overshoot of electrons (Ishibashi et al., 1994) in the depletion layer. Thus, with an appropriate UTC-PD design, electron diffusion time in the absorption layer mainly determines the device operation speed. In general, diffusion velocity is considered to be smaller than the drift velocity. However, in the absorption layer of the UTC-PD, the electron diffusion velocity can be very large for a relatively thin absorption layer due to the large minority mobility of electrons in p-InGaAs (Harmon et al., 1993). In addition, we can independently design the depletion layer and the absorption layer thicknesses in the UTC-PD structure. Thus, a very thin absorption layer can be used to attain an extremely high 3-dB bandwidth (f_{3dB}) without increasing the CR charging time. This is also an important advantage over the pin-PD, in which the CR charging time becomes significantly larger when the absorption layer thickness is excessively reduced (Kato et al., 1993).

The second advantage is the higher output saturation current due to much less space charge effect in the depletion layer, which also results from the high electron velocity in the depletion layer. In the pin-PD, the band profile is modified under a high-excitation condition (Willams et al., 1993) because of photo-generated carriers accumulated in the absorption layer as shown in Fig. 2(b). Thus, the decreased electric field reduces the carrier velocity, enhances the charge storage, and finally results in output current saturation. Although the situation is similar in the UTC-PD (Fig. 2(a)), the space charge consists of only

electrons whose velocity is much higher than that of holes even for the decreased electric field. Therefore, the output does not saturate until the current density becomes an order of magnitude higher than that for the pin-PD. Further, the velocity reduction of holes starts to occur even when the current density is relatively low. This is in contrast to the UTC-PD, where the prominent velocity reduction of electrons does not occur until the electric field becomes much smaller (Ishibashi et al., 1994). Therefore, the linearity range of the UTC-PD is much wider than that of the pin-PD.
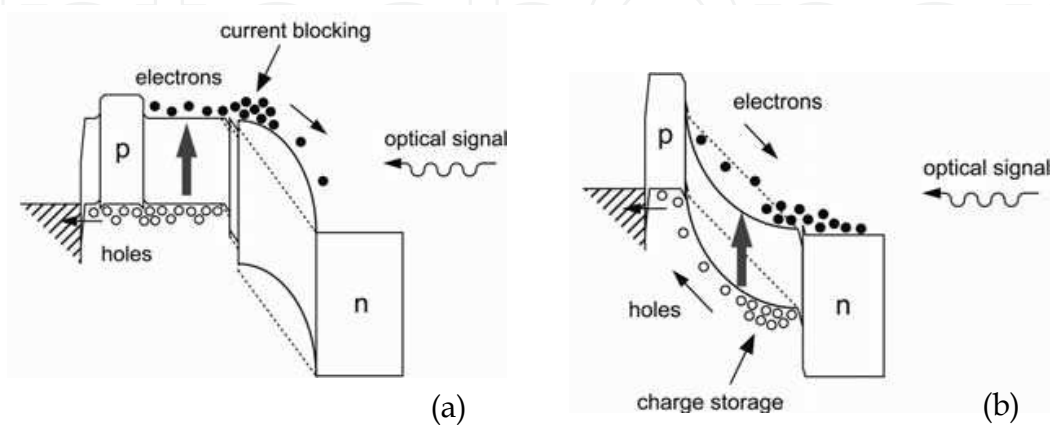
Fig. 2. Modified band diagram of a UTC-PD (a) and a pin-PD (b) at high optical input.

The third advantage is the capability of low-voltage operation. The high speed with high saturation output of the UTC-PD is maintained at a low (or even at zero) bias voltage (Ito et al., 2000a), because the high electron velocity in the depletion layer can be maintained at a relatively low electric field or even with the built-in field of the pn junction. This is in contrast to the large electric field required for holes to maintain relatively large drift velocity (Hill et al., 1987). A smaller operation voltage reduces power consumption, simplifies heat sinking, reduces biasing circuit cost, and improves reliability.
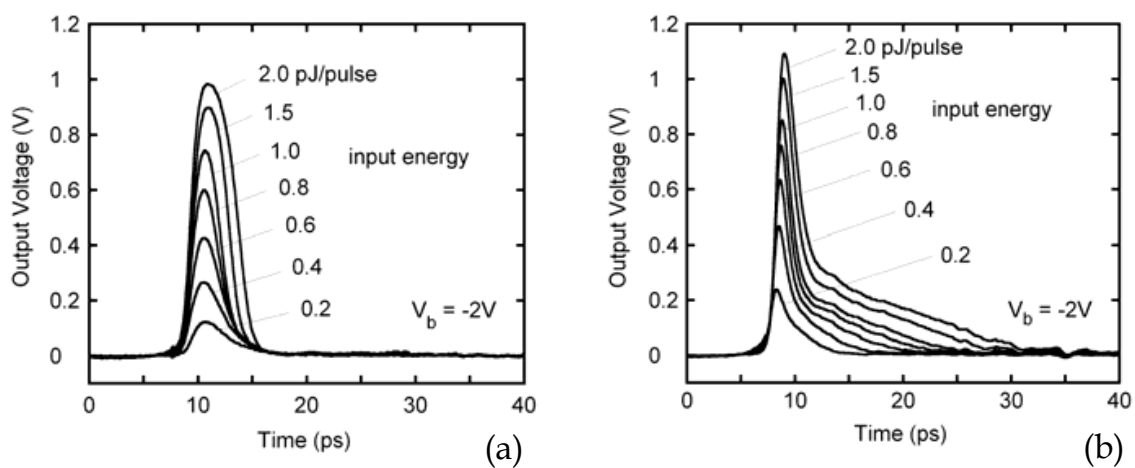

Fig. 3. Typical pulse photoresponses of a UTC-PD (a) and a pin-PD (b).

2.2 Basic characteristics
Figures 3(a) and (b) show typical output waveforms of the pulse photoresponse of a UTC-PD and a pin-PD (Furuta et al., 2000) measured using the electro-optic sampling technique.

In the UTC-PD, the output peak current increases linearly with increasing input energy, and the waveform does not significantly change until it reaches the saturation point. After the saturation occurs, the pulse width increases gradually. However, even at this stage, the fall time of the waveform does not prominently increase. The fast fall time even in the saturation region is attributed to the fast response of electrons accumulated in the depletion layer. On the other hand, the waveform of the pin-PD is quite different and it consists of two current components. The initial fast component is attributed to electron transport, and the slow tail is caused by hole transport. Especially, the full width of the hole-response increases drastically as the input energy increases. This is due to the stronger space charge effect of slow holes in the absorption layer as mentioned previously. The broadening of the waveform in turn results in severe degradation of the bandwidth and linearity of the pin-PD in a high excitation condition.
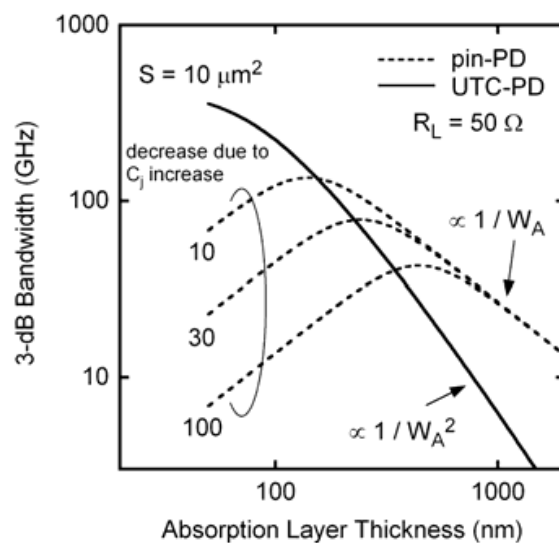
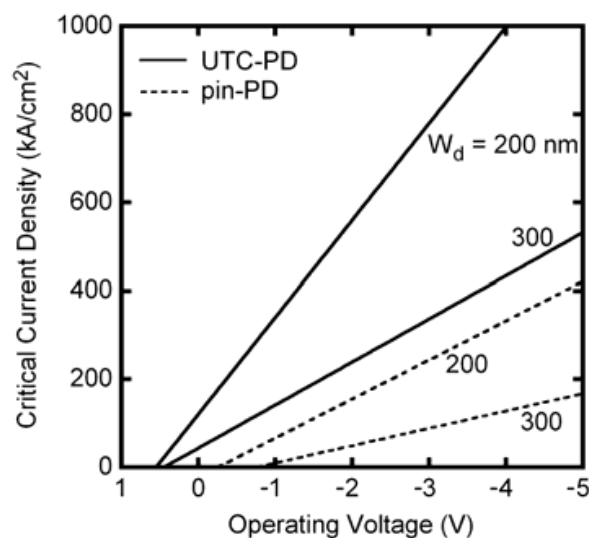Fig. 4. Calculated relationships between f_{3dB} and W_A for UTC-PD and pin-PDs.

Fig. 5. Calculated critical current densities against operating voltage for UTC-PDs and pin-PDs.

Figure 4 shows calculated f_{3dB} for the UTC-PD and pin-PD as a function of absorption layer thickness (W_A) (Ito et al., 2008). The f_{3dB} is basically proportional to $1/W_A^2$ for the UTC-PD and to $1/W_A$ for the pin-PD for thicker W_A. The former is due to the diffusive electron transport in the neutral absorption layer in the UTC-PD, and the latter is due to the drift motion of both carriers in the depletion layer of the pin-PD. If we try to increase the f_{3dB} of a pin-PD, we have to decrease W_A. However, as W_A is decreased, the bandwidth becomes smaller again at a certain point due to the junction capacitance (C_j) increase as shown by broken curves in Fig. 4. On the other hand, in the UTC-PD structure, the absorption layer and the collection layer are separated. Thus, f_{3dB} increases monotonically up to very thin W_A without C_j increase (solid curve in Fig. 4). Therefore, the prospective maximum f_{3dB} is much larger than that for the pin-PD. The maximum f_{3dB} reported for a UTC-PD is as high as 310 GHz (Ito et al., 2000b), which is twice as large as that reported for a pin-PD (Bach et al., 2007) operating at 1.55 μm.

As explained in the previous sub-section, the high output current of the UTC-PD is an important benefit over the conventional pin-PD. If we assume a simple velocity saturation model for both carriers (Ishibashi et al., 2000), the output current saturation starts to occur when the current density reaches a critical current density (J_c) at a critical electric filed (Tebbenham et al., 1975, Hill et al., 1987). Because of the larger saturation velocity and smaller critical electric field for electrons, J_c can be much larger for the UTC-PD than that for a pin-PD. Figure 5 shows the calculated J_c as a function of the operating voltage (V_b) for UTC-PDs and pin-PDs. Here, W_d is the depletion layer thickness. Although the ratio of J_c for the UTC-PD and the pin-PD depends on V_b, it lies in between about three and ten, and the ratio further increases when the W_d becomes larger. In an actual device, the charge distribution in the depletion layer is not uniform so that the output current saturation starts to occur at lower current density than in this calculation, especially in pin-PDs, resulting in a larger ratio of J_c. In addition, the pin-PD requires a certain negative bias voltage to work properly with the carrier velocity saturated, while the UTC-PD can be operated at zero or even positive bias voltages. A smaller W_d is further effective for expanding the operation area of the UTC-PD towards the positive bias voltage region.

For improving the UTC-PD performance, various modifications, including the structures proposed for pin-PDs and base-collector junctions of heterojunction bipolar transistors (Kroemer, 1982, Bowers et al., 1987, Ishibashi et al., 1988, Hafizi et al., 1993) are possible, and many of them have been applied to the UTC-PD structure. To decrease the electron traveling time in the absorption layer, the introduction of a quasi-field into the absorption layer by means of the band-gap grading and/or doping grading are effective (Ishibashi et al., 1997, Shimizu et al., 1998). For decreasing the electron traveling time in the collection layer, p-type doping or cliff-like structure (Shi et al., 2005) are suitable for optimizing the electric field profile. On the other hand, to increase the saturation current level, increased n-type doping in the collection layer (Shimizu et al., 1998, Li et al., 2004) is preferable. A combination of neutral and depleted absorption layers (Li et al., 2003, Muramoto et al., 2003) will increase the responsivity without considerably sacrificing the saturation current and operation speed. The use of dual-depletion region (Jun et al., 2006) is also effective in this modification to keep the high operation speed. Another way to improve the responsivity with the high operation speed maintained is to employ an external structure to guide the input light to the absorption layer at different angle, such as waveguide structure (Muramoto et al., 1998), evanescently coupled structure (Achouche et al., 2004), velocity-

matched distributed structure (Hirota et al., 2001), refracting facet structure (Fukano et al., 1999), and total reflection structure (Ito et al., 2000c).
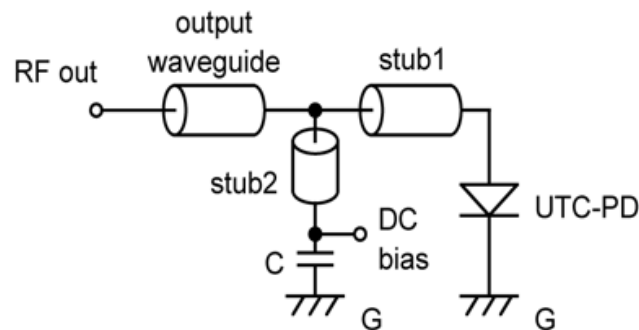

Fig. 6. A short-stub matching circuit integrated with a UTC-PD.

2.3 Circuit and package design

For efficiently utilizing the output power from the UTC-PD, the external circuit as well as the packaging is important. A resonant matching circuit is an effective element that can increase the maximum output power of a PD at desired frequencies. A typical example is a short-stub circuit (Ito et al., 2003a) containing two waveguides and a capacitor (Fig. 6). This circuit is a good solution for its simplicity, ease of integration with the UTC-PD, and limited numbers of optimizing parameters. It can change the effective output impedance, the resonant peak frequency, the peak output power, and the bandwidth. It also acts as a bias-tee circuit. All the elements fit within a standard-size chip, and can be fabricated without modifying the standard UTC-PD fabrication processes.

For a practical use, the device should be assembled in a module that is suitable for handling very high frequency signals. There are two possible approaches for transmitting very-high-frequency signals from a PD. One is to use a rectangular-waveguide-output module, and the other is to use a quasi-optic one. The waveguide-output approach is effective for transmitting the confined output signal to the objective. In addition, we can easily control the radiation pattern of the signal by using an appropriate external antenna. The drawback of this approach is that the bandwidth of the fundamental mode signal is essentially restricted by the waveguide nature. On the other hand, the key advantage of the quasi-optic module is its extremely-large bandwidth, and thus the full bandwidth can be covered with only one device. Drawbacks of this approach are that it requires a quasi-optic collimation system, the integration of a proper planar antenna with a PD, and proper tailoring of the radiation pattern for specific applications.

For the first approach, compact waveguide output UTC-PD modules have been developed. Figure 7 shows the one for operation in the J-band (220-325 GHz) (Ito et al. 2006). The output electrode of a matching-circuit-integrated UTC-PD is connected to an MSL-based waveguide fabricated on a quartz substrate, and it leads the output signal to a rectangular waveguide with a coupler. The module size is 12.7 mm x 30 mm x 10 mm, excluding the optical fiber and the bias connector. The modules for operation in the W-band (75 - 110 GHz) (Ito et al. 2002), F-band (90-140 GHz) (Ito et al. 2003b), and D-band (110 - 170 GHz) (Furuta et al. 2005) have also been developed. This package has an additional advantage for integrating other components for higher functionality (Ito et al., 2005a, 2010). Another possibility is that it can be operated at much higher frequency than its fundamental

frequency range. For example, the F-band module could be operated up to 813 GHz (Ito et al., 2004b), and the J-band module up to 650 GHz (Wakatsuki et al., 2008).
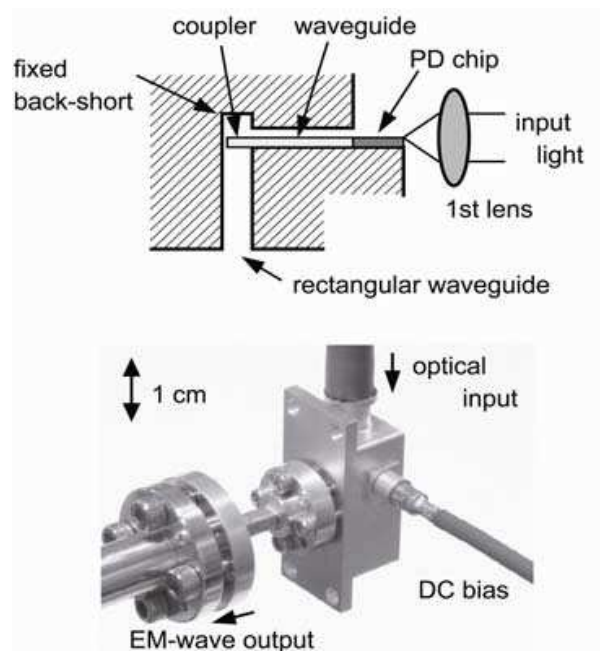

Fig. 7. Cross-sectional diagram and micrograph of a waveguide-output UTC-PD module.

For the second approach, a quasi-optic UTC-PD module (Ito et al., 2005b) shown in Fig. 8 has been developed. Here, the UTC-PD was integrated with a planar antenna, and the device was mounted on a hyper-hemispherical lens made of high-resistivity silicon to collimate the output EM wave.
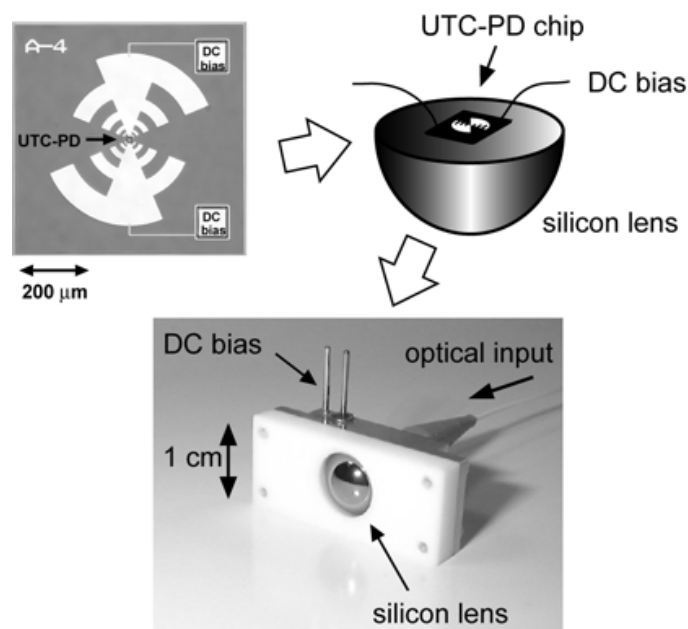
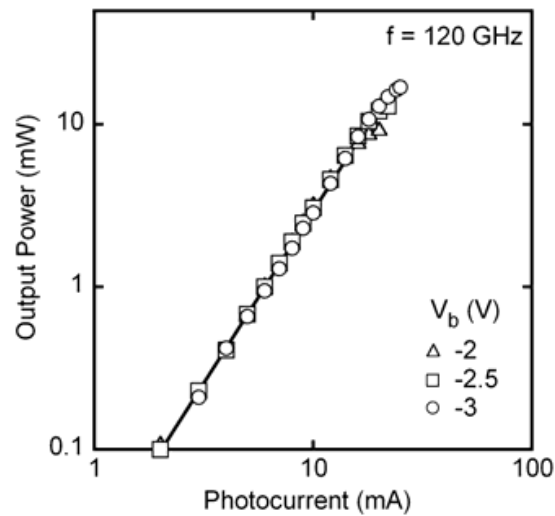Fig. 8. Assembly of the quasi-optical module employing a UTC-PD integrated with a log-periodic antenna.

Fig. 9. Relationship between measured mm-wave output power and the diode photocurrent for an F-band UTC-PD module at 120 GHz.

2.4 Generation of millimeter and THz waves

Figure 9 shows the relationship between measured millimeter-wave output power and photocurrent for the F-band UTC-PD module at 120 GHz (Ito et al. 2003b). A wide linearity range is maintained up to a very high mm-wave output power of over 10 mW. The saturation point of the output power increased with increasing bias voltage, and the maximum output power of 17 mW was obtained at a bias voltage of -3 V with a photocurrent of 25 mA.

Figure 10 shows the output power against frequency for a J-band UTC-PD module at a photocurrent of 20 mA (Wakatsuki et al., 2008). The output 3-dB down bandwidth was about 120 GHz, and the 10-dB bandwidth was about 300 GHz. Here, most of the frequency variation is that of the integrated matching circuit. The steep decrease of the output power
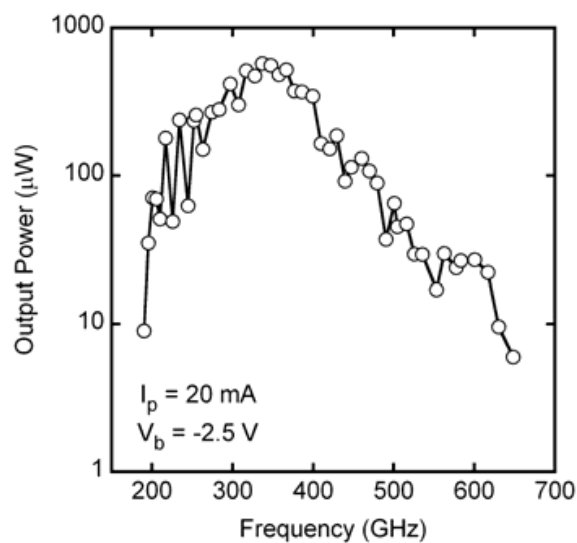

Fig. 10. Output powers against frequency for a J-band UTC-PD module designed for an over-mode operation.

at the low-frequency side is due to the cut-off characteristics of the WR-3 waveguide (at 173 GHz). In the high-frequency region, on the other hand, the output power decrease with increasing frequency is more gradual. This is because there is no cut-off frequency for the fundamental mode signal and the higher-order-mode output is also possible in the frequency range above 347 GHz.
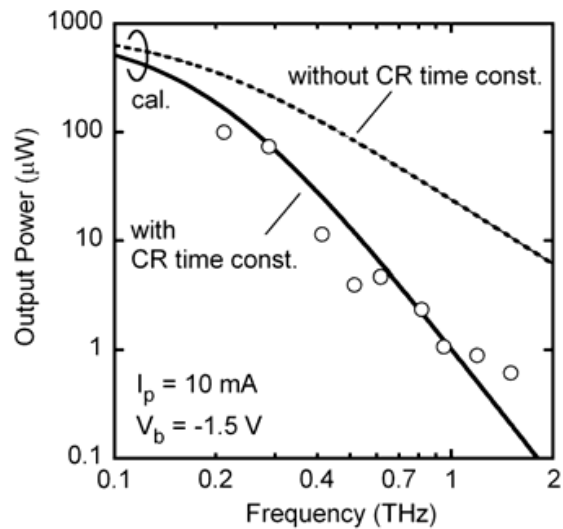
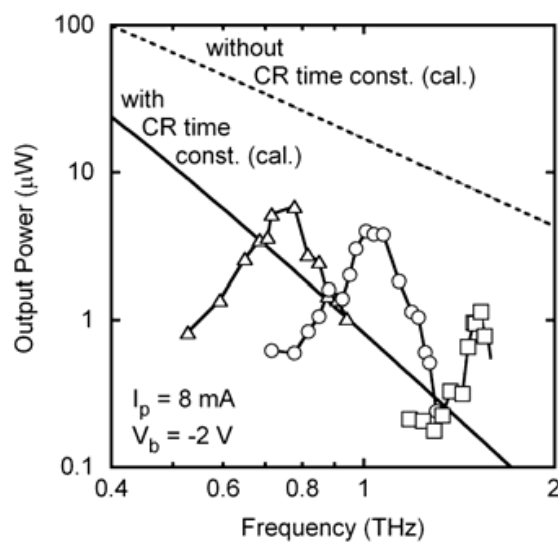Fig. 11. Frequency dependence of the output power from a quasi-optic UTC-PD module.

Fig. 12. Output powers against frequency for UTC-PDs integrated with resonant twin-dipole antennas.

As an example for the quasi optical approach, the UTC-PD was integrated with a wideband self-complementary log-periodic antenna (Ito et al., 2005b) as shown in Fig. 8. Figure 11 shows the frequency characteristics of the output power from the fabricated quasi-optical module at a photocurrent of 10 mA. The output power decreased gradually with increasing frequency, and the sub-mm waves were detected at frequencies of up to 1.5 THz. The solid curve in the figure is a calculation, which only takes into account the CR-limited and transit-time-limited bandwidth of the UTC-PD with a constant loss. The experimental result agrees

well with the calculation, indicating that only the device parameters of the PD determine the basic frequency dependence. Thus, if we compensate for the influence of the CR time constant by employing a resonant matching circuit, it will be possible to increase the output power toward the level indicated by the broken curve in the figure, where only the transit-time-limited bandwidth is considered.

For this purpose, UTC-PDs integrating resonant twin-dipole planar antennas were also fabricated (Nakajima et al., 2004). Figure 12 shows the frequency characteristics of the fabricated devices for a photocurrent of 8 mA. The calculations for the wideband UTC-PD integrating a log-periodic antenna at the same photocurrent are also shown for comparison. The output power for each resonant device exhibits peaking behavior at different frequencies, namely, at 0.78, 1.04, and 1.53 THz. The peak output values are considerably higher than the output power from the wideband device for the same photocurrent, indicating the effectiveness of the resonant design. The peak output powers lie in between the two curves, one is with CR time constant and the other is without. This is because there is a tradeoff between the bandwidth and peak output power even in the resonant design so that the influence of the CR time constant is only partially compensated by the resonant circuit. Figure 13 shows the relationship between the detected output power and the photocurrent at 1.04 THz for the device having a peak at the same frequency with a bias voltage of -2 V. The inset is a micrograph of a UTC-PD with a resonant twin-dipole antenna. The output power increased linearly in proportion to the square of the photocurrent, and the maximum output power obtained was 10.9 μW at a photocurrent of 14 mA.
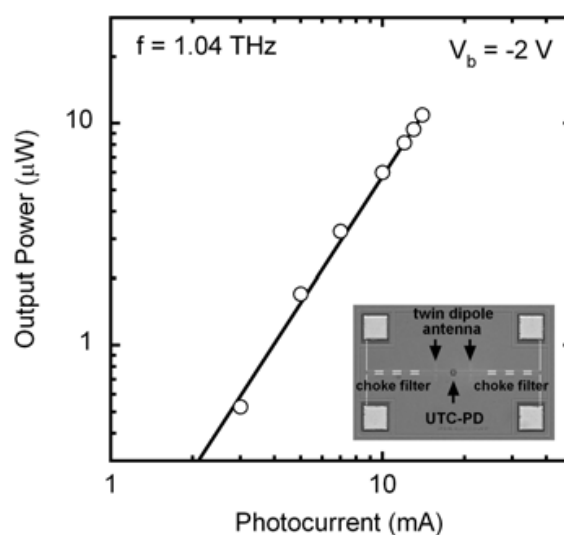

Fig. 13. Output powers against photocurrent for a UTC-PD integrated with a twin-dipole antenna having a resonant peak at 1.04 THz.

Figure 14 compares reported RF output powers for UTC-PDs (Ito et al., 2005b), pin-PDs (Huggard et al., 2002, Stöhr et at., 2003, Malcoci et al., 2004) and LT-GaAs photomixers (Duffy et al., 2001) with wideband designs. The results for narrowband UTC-PDs (Ito et al., 2003b, Nakajima et al., 2004, Wakatsuki et al., 2008, Rouvalis et al., 2010) are also shown for comparison. Although the output power for each type of device decreases inversely proportional to the fourth power of the frequency, the results for UTC-PDs are about two orders of magnitude higher than those for pin-PDs. This difference is mainly due to the

high saturation current levels of the UTC-PD. The output power of the UTC-PD is even higher than those reported for LT-GaAs photomixers. These results clearly indicate that the UTC-PD is a promising device for generating a continuous terahertz wave with a high output power. The output powers of narrowband UTC-PDs are even higher than those with wideband design. However, they also tend to decrease with increasing frequency along the results for devices with wideband design. This indicates that, even for a device with a resonant design, it is essential to improve the intrinsic device performance for further increasing the output power of the UTC-PD.
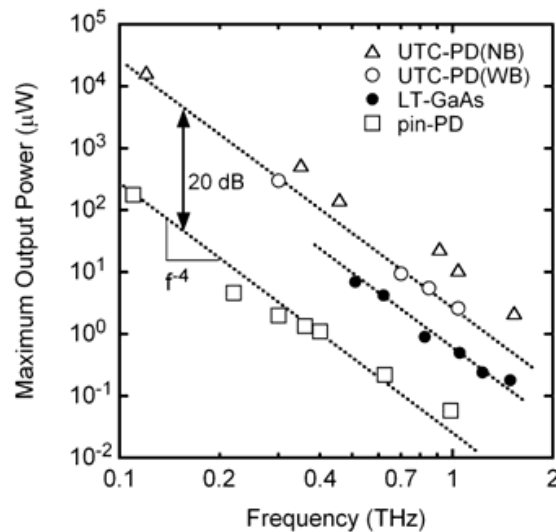

Fig. 14.Comparison of reported mm-/sub-mm-wave output powers against the operation frequency for UTC-PDs, pin-PDs, and LT-GaAs photomixers.

Application	Generator	Detector
Communications	**Photonic emitter using UTC-PD**	Schottky-barrier diode detector
Spectroscopy Active I	**Photonic emitter using UTC-PD**	Schottky-barrier diode detector
Active II	**Photonic emitter using UTC-PD**	SIS mixer with **photonic LO**
Active III	**Photonic emitter using UTC-PD**	**Photonic mixer using UTC-PD**
Passive	NA	SIS mixer with **photonic LO**
Imaging	**Photonic noise source using UTC-PD**	Schottky-barrier diode detector

Table 1. Summary of several applications using UTC-PDs.

3. Applications of the UTC-PD

Table 1 summarizes applications of photonically generated millimeter and terahertz waves in wireless communications, spectroscopic measurement systems and imaging systems. In wireless communications, UTC-PDs are used to generate millimeter and sub-millimeter waves in transmitters. In spectroscopy applications, UTC-PDs are employed as mixers in detectors as well as in generators. Photonically generated noise signals can be used as illuminators in the active imaging systems. In the following, these applications are described in more detail.

3.1 Wireless communications

Here, we describe wireless link systems using two bands; one is 120-GHz band and the other is 300-GHz band. One of common concerns when we use >100-GHz radio waves for wireless communications is a large propagation loss in the air. From 100 to 300 GHz, there are three valleys, where the attenuation is a local minimum; 75-100 GHz, 120-160 GHz, and 220-320 GHz. Our initial choice is the 120-GHz band centered at 125 GHz.

A block diagram of a 120-GHz-band wireless link system with 10-Gbit/s transmission capability is shown in Fig. 15 (Hirata et al. 2003, 2006, 2008, Suzuki et al., 2005). A photonic millimeter-wave generator is used in the transmitter. An optical millimeter-wave source generates optical subcarrier signals whose intensity is modulated at 125 GHz. An optical intensity (ASK) modulator (MZM) modulates the optical subcarrier signal using data signals. The modulated subcarrier signal is amplified by an optical amplifier (EDFA) and input to the high-power UTC-PD. The UTC-PD converts the optical signals into millimeter-wave signals, which are amplified and radiated toward the receiver via an antenna. The received millimeter-wave signals are amplified and demodulated by a simple envelope detection scheme, for example. The millimeter-wave receiver is composed of all-electronic devices such as pre-amplifier and Schottky-barrier diode (SBD) detector using InP-HEMT technology.
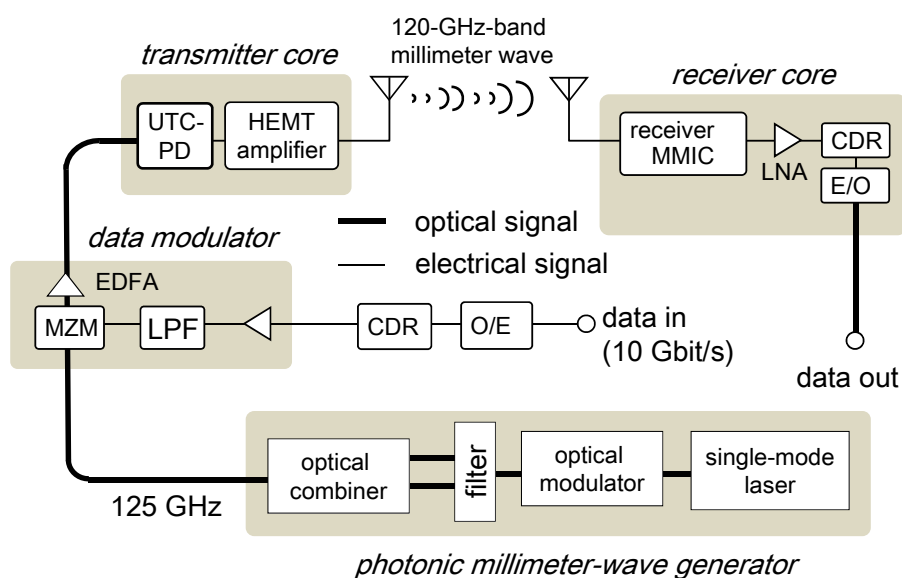

Fig. 15. Block diagram of 120-GHz band wireless link system using the UTC-PD in the transmitter.

The promising application of the above 10-Gbit/s wireless link is found in the broadcasting industry. A wireless link system that can transmit "uncompressed" high-definition television (HDTV) signals has been strongly desired, because TV program production based on the HDTV standard is spreading rapidly in TV stations due to the launch of digital TV broadcasting all over the world. An uncompressed HDTV signal (HD-SDI: high definition serial digital interface) requires a data rate of 1.5 Gbit/s per channel. Commercial wireless links using 60-GHz-band MMWs have a data rate of over 1.5 Gbit/s and thus a capability of transmitting one channel of uncompressed HD-SDI signals. However, large-scale live relay broadcasts, such as golf tournaments and music concerts, requires multiple channels of uncompressed HD-SDI signals. The 120-GHz-band system allows up to 6 channels of uncompressed HDTV material to be sent over a wireless link with no latency.

For such a purpose, this link uses a high-gain (~50 dBi) Cassegrain antenna, and can support the optical network standards of both 10 GbE (10.3 Gbit/s) and OC-192 (9.95 Gbit/s) with a bit error rate of 10^{-12}.

To increase the bit rate to 20-40 Gb/s or more, use of higher carrier frequencies of over 200 GHz is promising. In particular, the use of terahertz waves at frequencies above 275 GHz has attracted a great deal of interest for wireless communications. This is mainly because that these frequency spectra have not yet been allocated to specific applications and thus we can possibly make use of extreme bandwidth for high-speed communications.
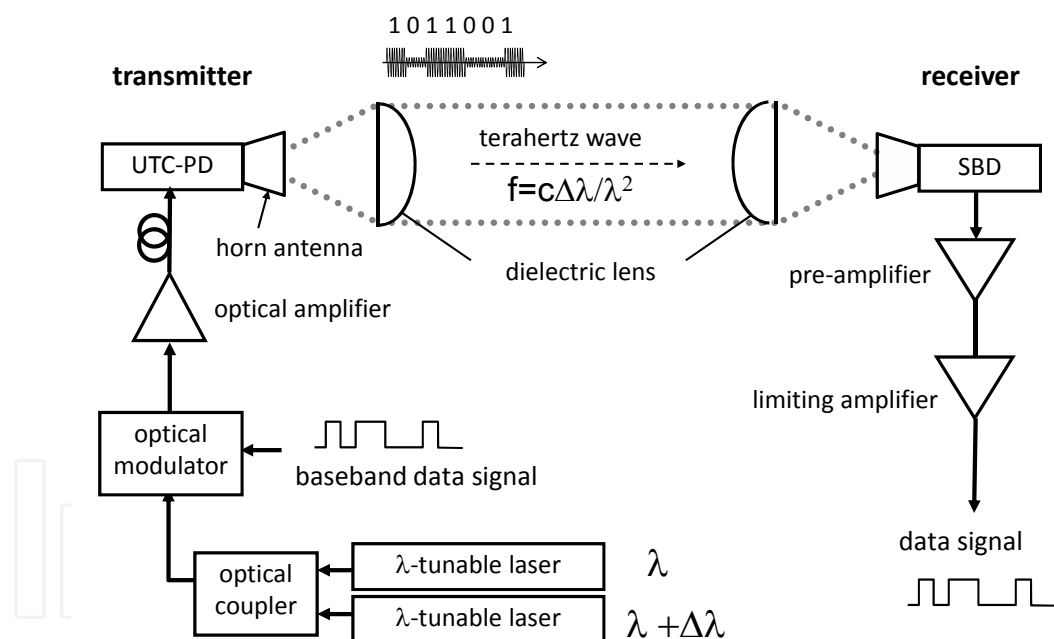

Fig. 16. Block diagram of 300-GHz band wireless link system using the UTC-PD in the transmitter.

Figure 16 shows a block diagram of 300-400 GHz band system using a photonics-based transmitter (Nagatsuma et al., 2009a, 2010a). This system is intended for use in short-distance (<10 m) applications, since there are no amplifiers. An optical RF signal is generated by heterodyning the two wavelengths of light from the wavelength-tunable light sources. The optical signal is digitally modulated by the optical intensity modulator driven by the pulse pattern generator (PPG). Finally, the optical signal is converted to an electrical signal by the UTC-PD. The terahertz wave is emitted to the free space via a horn antenna

with a gain of 25 dBi, and it is well collimated by a 2-inch-diameter Teflon lens. The receiver consists of a Schottky barrier diode (SBD) and an IF filter followed by a low-noise pre-amplifier and a limiting amplifier.
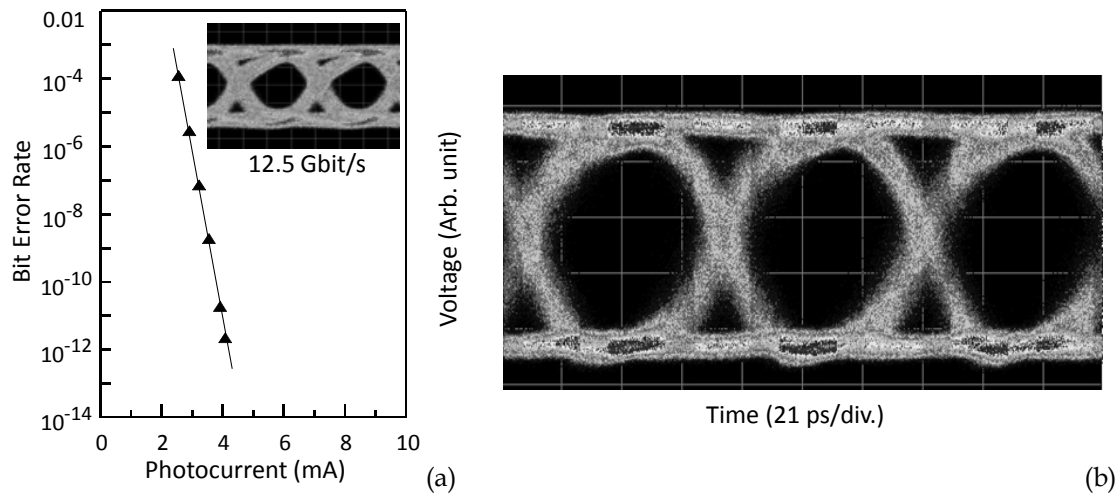

Fig. 17. (a) BER characteristics of 300-GHz wireless link. (b) 14-Gbit/s eye diagram.

Figure 17(a) shows BER characteristics at 12.5 Gbit/s with a carrier frequency of 300 GHz. Horizontal axis is a photocurrent of the transmitter. An error-free transmission at 12.5 Gbit/s has been achieved with 4-mA current, which corresponds to the transmitter output of around 10 µW. Currently, the upper limits in the bit rate of PPG and BER tester are 14 Gbit/s and 12.5 Gbit/s, respectively. Figure 17(b) shows the eye diagram at 14 Gbit/s. Although the BER could not be measured, an error-free transmission was confirmed from the clear eye opening. Based on the design, >20Gbit/s will be feasible.
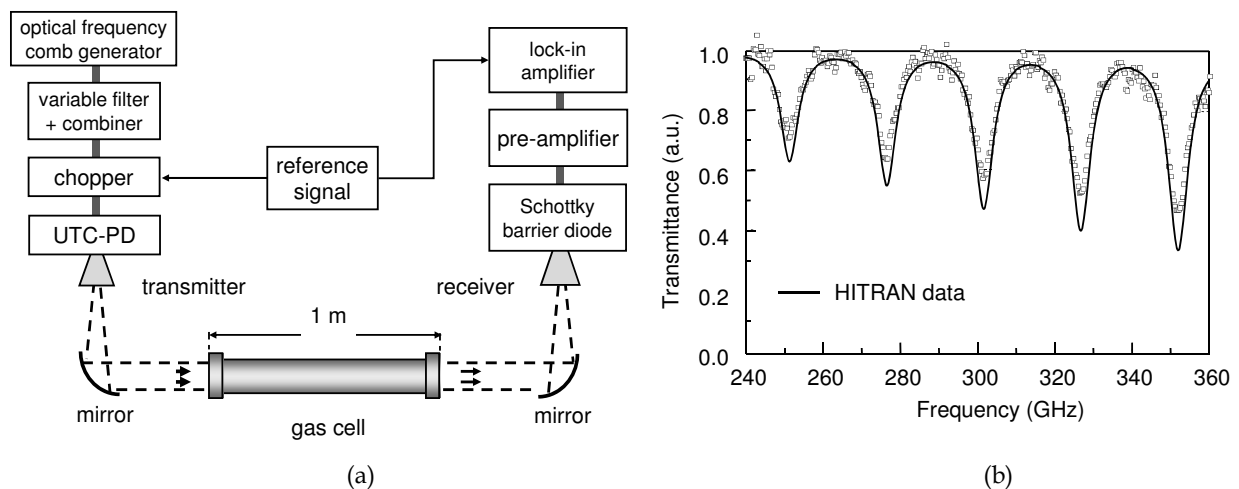

Fig. 18. Block diagram of the spectroscopy system using the UTC-PD and the Schottky barrier diode in the transmitter and receiver, respectively. (b) Experimental results.

3.2 Spectroscopy
In the following, we describe measurement results obtained by spectroscopy systems using photonic millimeter-/terahertz-wave emitters in combination with the different detection

techniques. First, using the photonic millimeter-/terahertz-wave generator and the direct detection scheme, simple spectroscopic measurements were demonstrated in the frequency range between 240 and 360 GHz, as shown in Fig. 18 (Song et al., 2008a). The sample under the test was a mixture of N_2O and N_2 in the ratio of 3:1 (75 %), and it was filled in a 1-m long gas cell under atmospheric pressure. The experimental setup is shown in Fig. 18(a). The millimeter-/terahertz-wave signal generator was computer controlled to sweep the frequency and the optical millimeter-/terahertz-wave signal before the UTC-PD was intensity modulated at a frequency of 10 kHz. Then the generated signal was radiated and collimated with a diagonal horn antenna and a gold-coated off-axis parabolic mirror, respectively. The signal transmitted through the gas cell was received with a Schottky barrier diode detector followed by a lock-in amplifier tuned to 10 kHz.

The measured transmittance for the gas is plotted in Fig. 18(b) with the simulated results based on the HITRAN (**hi**gh-resolution **tran**smission molecular absorption) database (HITRAN homepage). As can be seen, the positions and tendency of the magnitude and the shape of absorption peaks from the measurement coincide well with those of HITRAN. The measurement bandwidth can be extended by using a photomixer and a receiver, which are integrated with broadband antennas (Hirata et al., 2002).

The ultralow-noise characteristics of the photonically generated millimeter-/terahertz-wave signal were verified through their application to the local oscillator (LO) for the superconducting mixers in heterodyne receivers, which operate at 4.2 K. Figure 19(a) shows an experimental setup of the cryogenic receiver pumped by the photonic LO signal (Kohjiro et al., 2008). Measured noise temperatures of the receiver with a photonic LO and a conventional Gunn LO are plotted in the frequency range from 180 GHz to 500 GHz. Three Gunn oscillators were required to cover this frequency range even in part, while it was fully covered by the single photonic LO. As shown in Fig. 19(b), the noise temperature was as low as 300 K, which corresponds to better than pico-watt sensitivity over an octave frequency range.
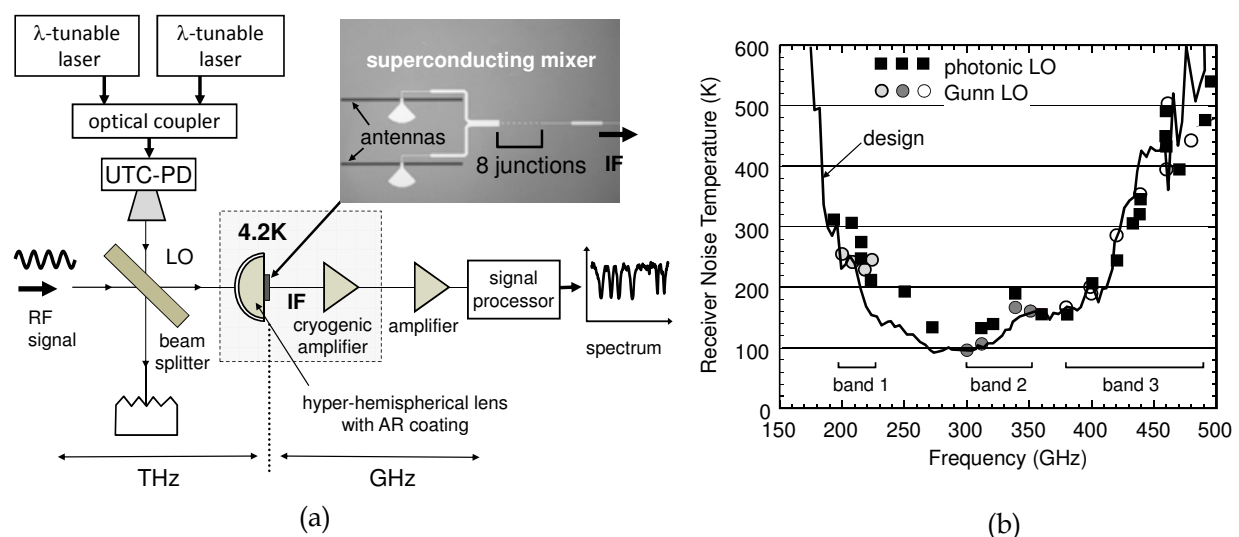

Fig. 19. Experimental setup of the cryogenic receiver pumped by photonic local oscillator. (b) Frequency characteristic of the noise temperature.
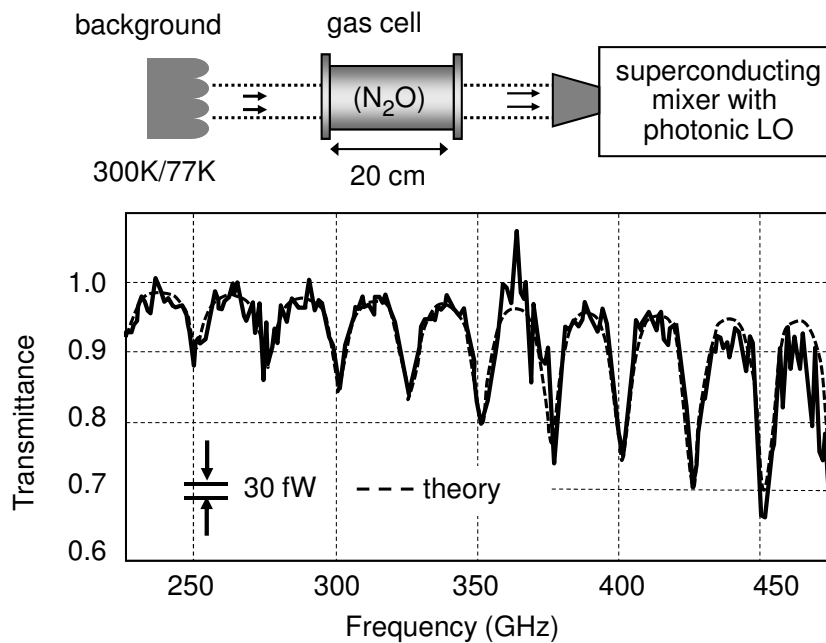
Fig. 20. Passive spectroscopic measurement of gas.

This receiver was successfully applied to the passive spectroscopy of gasses, as shown in Fig. 20. By using black-body radiation sources at 77 K and 300 K, the absorption can be calibrated accurately. It takes 1 - 2 minutes to scan the frequency range from 200 GHz to 450 GHz.

By combining the above ultra-sensitive SIS receiver pumped by the photonic LO with the photonic millimeter-wave sweeper, stand-off detection of toxic and/or dangerous gasses such as CO, CO_2, HCN, HCl, SO_x, NO_x, was successfully performed (Oh et al., 2009).

In addition to the generator, the UTC-PD can be used as a detector. Figure 21 shows the operation principle of the photodiodes as terahertz-wave detectors. There are two operation modes with different voltage-bias conditions; one is a square-law detector under the forward bias condition, and the other is a down-converter under the reverse bias. In case of down-conversion (Fig. 21(b)), the origin of the nonlinearity of the UTC-PD can be explained by the dynamic capacitance associated with charge storage in the photo-absorption layer (Fushimi et al., 2004). Mixing between the input terahertz wave, f_{RF}, and the local oscillator (LO) signal, f_{LO}, photonically generated in the photodiode leads to the intermediate frequency, f_{IF}.
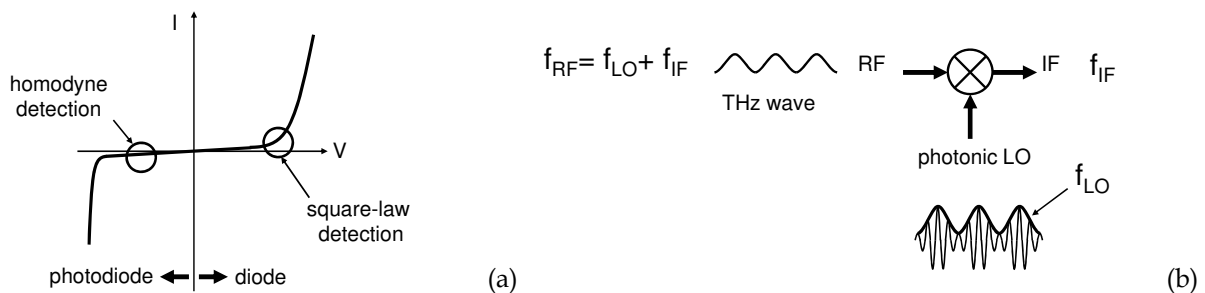

Fig. 21. Operation principle of the UTC-PD for receivers as a down-converter and a square-law detector.
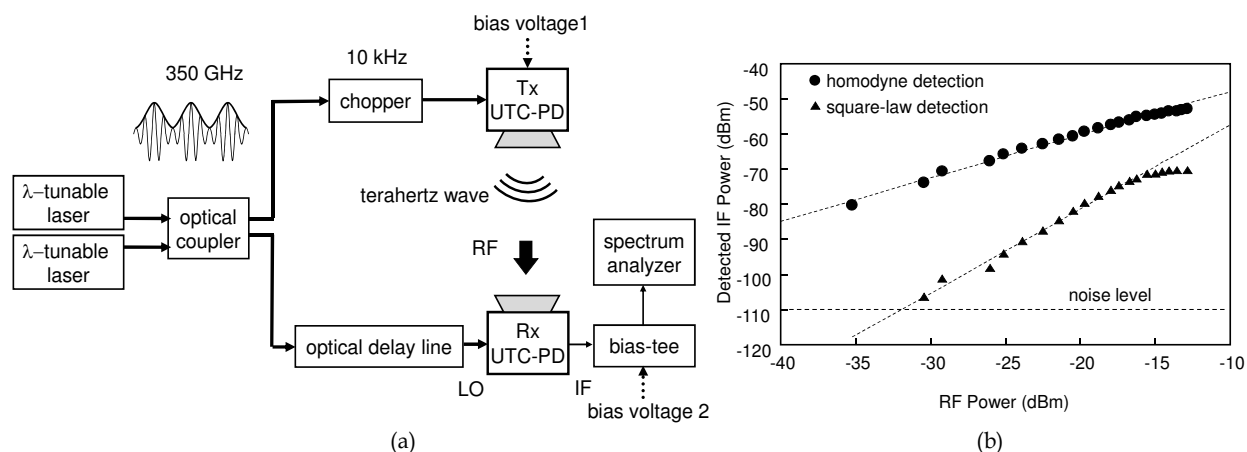
Fig. 22. (a) Block diagram of the spectroscopy system using the UTC-PDs both in the transmitter and receiver. (b) Detection characteristics of the UTC-PD as a down-converter and a square-law detector.

Figure 22(a) shows a block diagram of the CW THz spectrometer consisting of the transmitter (Tx) and the receiver (Rx) based on the down-conversion (Nagatsuma et al., 2010b). This coherent system is often referred to as "homodyne" detection system (Ducournau et al., 2009). Optical delay line was used to maximize the intermediate frequency signal at 10 kHz. Dependence of the IF power on the input RF power at 350 GHz was compared between the homodyne detection and the square-law detection as shown in Fig. 22(b). For the homodyne detection, the optical LO power was set to -15.5 dBm, which is an optimum condition experimentally confirmed. Maximum S/N (ratio of IF power to noise level) is 39 dB for the square-law detection, while it is 58 dB for the homodyne detection. This corresponds to the difference in the maximum conversion efficiency is 19 dB. Since the available output power from the UTC-PD is more than -4 dBm, about 20-dB loss in the transmission between transmitter and receiver and as well as in the object under test is still allowable for the actual spectroscopy. In addition, since the slope in the relationship between the RF power and the IF power is smaller for the homodyne detection, loss caused in the object and transmission has less effect, which may be a merit of the homodyne detection scheme.
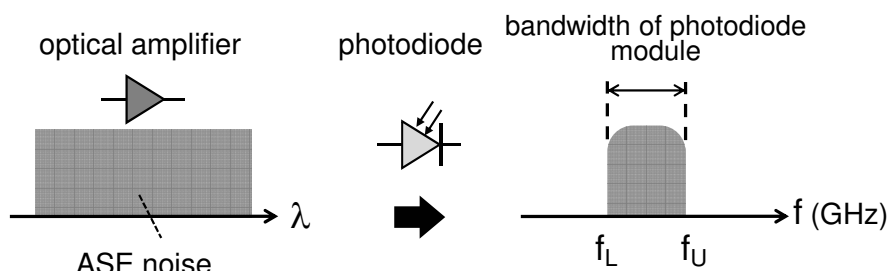
3.3 Imaging

Millimeter-wave and terahertz-wave imaging has been extensively studied and deployed in numerous areas such as material inspection, non-destructive testing, and security applications (Chan et al., 2007). Between continuous-wave (CW) and pulsed-wave imaging systems, the CW imaging can be faster, more compact, cost-effective and simpler to operate. However, mono-chromatic waves cause interference effect due to reflection of waves at any boundary in the materials under inspection and components used such as lenses and mirrors, which leads to significant degradation in image quality and effective spatial resolution (Redo-Sanchez et al., 2006).

Here, we present a new approach to achieving high-quality image with use of photonically-generated incoherent millimeter-wave noise signals (Nagatsuma et al., 2009b). Figure 23(a)

shows a block diagram of transmission-type millimeter-wave imaging system using incoherent illumination source. The amplified spontaneous emission (ASE) noise from Er-doped fiber amplifier is delivered to the UTC-PD. The UTC-PD converts the optical noise to the electrical noise (Fig. 23(b)). Then, the noise is radiated into free space via a horn antenna.
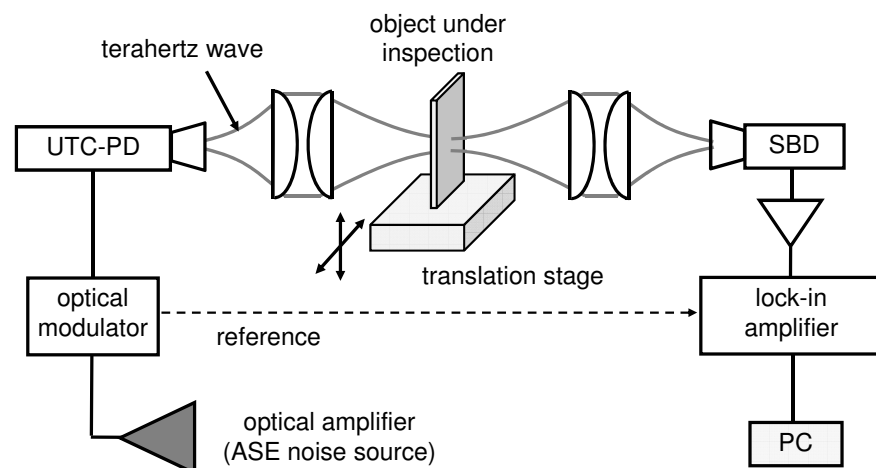
(a)

(b)

Fig. 23. (a) Block diagram of the imaging system using an incoherent noise source.
(b) Mechanism of the noise generation using the photodiode.

In order to verify the effectiveness of the proposed technique, the imaging of a clip hidden in the paper envelope was conducted as shown in Fig. 24(a). For comparison, the millimeter-wave images obtained by a monochromatic 320-GHz signal are also shown in Figs. 24(b). The 320-GHz signal was generated by injecting two optical signals with a frequency difference of 320 GHz from two wavelength-tunable lasers into the UTC-PD. The linewidth of the generated millimeter-wave signal is about 10 MHz. Even in the case of the thin envelope, interference effect caused artifact near the clip. As clearly shown in Fig. 24, the interference effect has been dramatically reduced by the incoherent source without scarifying the spatial resolution.

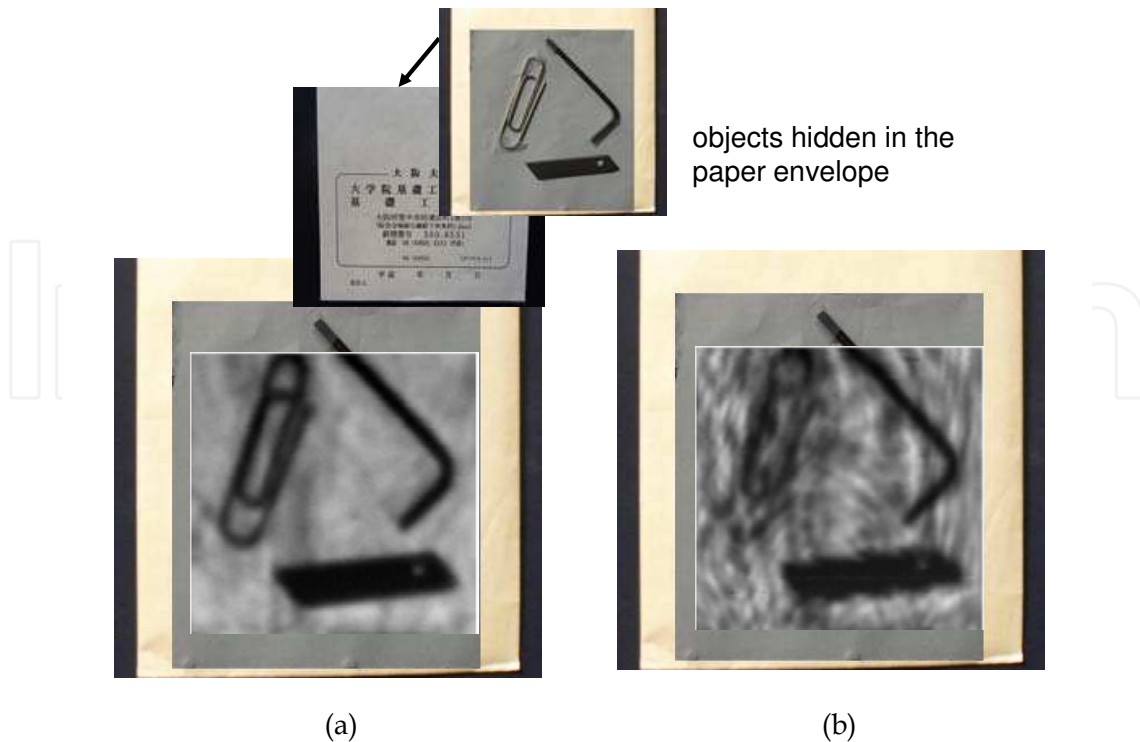Song et al. also demonstrated the effectiveness of noise in the spectroscopic measurement (Song et al., 2008b).

objects hidden in the paper envelope

(a)   (b)

Fig. 24. Comparison of images obtained by noise source (a) and coherent source at 320 GHz (b).

4. Conclusions

The combination of radio-wave and photonics technologies is an effective way to explore electromagnetic waves in the undeveloped millimeter-/terahertz-wave frequency regions. In this article, we have described photonic generation of continuous millimeter-/terahertz-wave signals using UTC-PDs and their applications to communications, spectroscopic measurement and imaging. Currently, the maximum available output power at 1 THz is around 10 μW. Improvement of photodiode performance in terms of saturation current and thermal management as well as efficient RF coupling between the photodiode and the antenna front-end will allow a single device to emit powers on a level of 100 μW at 1 THz. The power combining technique using an array of photodiodes promises to increase the output power up to the 1-mW level. Thus, photodiode-based CW millimeter-/terahertz-wave technologies are expected to be at the forefront of a new generation of more compact, versatile and cost-effective millimeter-and terahertz-wave systems.

5. Acknowledgments

6. References

Achouche, M.; Magnin, V.; Harari, J.; Lelarge, F.; Derouin, E.; Jany, C.; Carpentier, D.; Blache, F. & Decoster, D. (2004). High performance evanescent edge coupled waveguide unitraveling-carrier photodiodes for >40-Gb/s optical receivers, *IEEE Photonics Technol. Lett.*, Vol. 16, No. 2, pp. 584-586.

Bach, H.-G. (2007). Ultrafast waveguide-integrated pin-photodiodes and photonic mixers from GHz to THz range, *Proc. 33rd European Conf. and Exhibition on Optical Communication*, Vol. 5, pp. 247-250.

Bowers, J. E. & Burrus, Jr. C. A. (1987). Ultrawide-band long-wavelength p-i-n photodetectors, *IEEE J. Lightwave Tech.*, Vol. 5, No. 10, pp. 1339-1350.

Chan, W. L.; Deibel, J. & Mittleman, D. M. (2007). Imaging with terahertz radiation", *Rep. Prog. Phys.*, Vol. 70, pp. 1325-1379.

Ducournau, G., Beck, A., Blary, K., Peytavit, E., Zaknoune, M., Akalin, T., Lampin, J.-F., Martin, M., & Mangeney, J. (2009). All-Fiber continuous wave coherent homodyne terahertz spectrometer operating at 1.55 μm wavelengths, *Proc. 2009 Infrared, Millimeter and Terahertz Waves (IRMMW-THz 2009)*, T4A02.0362.

Duffy, S. M.; Verghese, S.; McIntosh, K. A.; Jackson, A.; Gossard, A. C. & Matsuura, S. (2001). Accurate modeling of dual dipole and slot elements used with photomixers for coherent terahertz output power," *IEEE Trans. Microwave Theory and Tech.*, Vol. 49, pp. 1032-1038.

Fukano, H.; Muramoto, Y.; Takahata, K. & Matsuoka, Y. (1999) High-efficiency edge-illuminated uni-traveling-carrier-structure refracting-facet photodiode, *Electron. Lett.*, Vol. 35, pp. 1664-1665.

Furuta, F.; Ito, H. & Ishibashi, T. (2000). Photocurrent dynamics of uni-traveling-carrier and conventional pin-photodiodes, *Inst. Phys. Conf. Ser.*, No. 166, pp. 419-422.

Furuta, T.; Ito, T.; Muramoto, Y.; Ito, H.; Tokumitsu, M. & Ishibashi, T. (2005). "D-band rectangular-waveguide-output uni-traveling-carrier photodiode modules, *Electron. Lett.*, Vol. 41, pp. 715-716.

Fushimi, H.; Furuta, T.; Ishibashi, T. & Ito, H. (2004). Photoresponse nonlinearity of a uni-traveling-carrier photodiode and its application to optoelectronic millimeter-wave mixing in 60 GHz band, *Jap. J. Appl. Phys.*, vol. 43, no. 7B, pp. L966-968.

Hafizi, H.; Liu, T.; Rensch, D. B. & Stanchina, W. E. (1993). Effects of collector doping on DC and RF performance of AlInAs/GaInAs/InP double heterojunction bipolar transistors, *IEEE Trans. Electron Dev.*, Vol. 40, No. 11., pp. 2122-2123.

Harmon, E. S.; Lovejoy, M. L.; Melloch, M. R.; Lundstrom, M. S.; Ritter, D. & Hamm, R. A. (1993). Minority-carrier mobility enhancement in p+ InGaAs lattice matched to InP, *Appl. Phys. Lett.*, Vol. 63, pp. 636-638.

Hill, P.; Schlafer, J.; Powazinik, W.; Urban, M.; Eichen, E. & Olshansky, R. (1987). Measurement of hole velocity in n-type InGaAs, *Appl. Phys. Lett.*, Vol. 50, pp. 1260-1262.

Hirata, A.; Nagatsuma, T.; Yano, R.; Ito, H.; Furuta, T.; Hirota, Y.; Ishibashi, T; Matsuo, H.; Ueda, A.; Noguchi, T.; Sekimoto, Y. ; Ishiguro, M. & Matsuura, S. (2002). Output

power measurement of photonic millimeter-wave and sub-millimeter-wave emitter at 100-800 GHz, *Electron. Lett.*, Vol. 38, No. 15, pp. 989-800.

Hirata, A.; Harada, M. & Nagatsuma, T. (2003). 120-GHz wireless link using photonic techniques for generation, modulation, and emission of millimeter-wave signals," *IEEE J. Lightwave Technology*, Vol. 21, No. 10, pp. 2145-2153.

Hirata, A.; Kosugi, T.; Takahashi, H.; Yamaguchi, R.; Nakajima, F.; Furuta, T.; Ito, H.; Sugahara, H.; Sato, Y. & Nagatsuma, T. (2006). 120-GHz-band millimeter-wave photonic wireless link for 10-Gb/s data transmission," *IEEE Trans. Microwave Theory Tech.*, vol. 54, no. 5, pp. 1937-1944.

Hirata, A.; Takahashi, H.; Yamaguchi, R.; Kosugi, T.; Murata, K.; Nagatsuma, T.; Kukutsu, N. & Kado, Y. (2008). Transmission characteristics of 120-GHz-band wireless link using radio-on-fiber technologies, *J. Lightwave Technol.*, Vol. 26, No. 15, pp. 2338-2344.

Hirota, Y.; Ishibashi, T. & Ito, H. (2001). 1.55-μm wavelength periodic traveling-wave photodetector fabricated using unitraveling-carrier photodiode structures, *J. Lightwave Technol.*, Vol. 19, No. 11, pp. 1751-1758.

HITRAN homepage, http://cfa-www.harvard.edu/hitran/welcometop.html

Huggard, P. G.; Ellison, B. N.; Shen, P.; Gomes, N. J.; Davis, P. A.; Shillue, W. P.; Vaccari, A. & Payne, J. M. (2002). Generation of millimetre and sub-millimetre waves by photomixing in 1.55 μm wavelength photodiode, *Electron. Lett.*, Vol. 38, pp. 327-328.

Ishibashi T. & Yamauchi, Y. (1988). A possible near-ballistic collection in an AlGaAs/GaAs HBT with a modified collector structure, *IEEE Trans. Electron Dev.*, Vol. 35, No. 4, pp. 401-404.

Ishibashi, T. (1994). High speed heterostructure devices, In: *Semiconductors and Semimetals*, Vol. 41, Chap. 5, p. 333, Academic Press, San Diego.

Ishibashi, T.; Shimizu, N.; Kodama, S.; Ito, H.; Nagatsuma, T. & Furuta, T. (1997). Uni-traveling-carrier photodiodes, *Tech. Dig. Ultrafast Electronics and Optoelectronics (1997 OSA Spring Topical Meeting)*, pp. 166-168, Incline Village, Nevada.

Ishibashi, T.; Furuta, T.; Fushimi, H.; Kodama, S.; Ito, H.; Nagatsuma, T.; Shimizu, N. & Miyamoto, Y. (2000). InP/InGaAs uni-traveling-carrier photodiodes, *IEICE Trans. Electron.*, Vol. E83-C, No. 6, pp. 938-949.

Ito, H.; Furuta, T.; Kodama S. & Ishibashi, T. (2000a). Zero-bias high-speed and high-output-voltage operation of cascade-twin uni-travelling-carrier photodiode, *Electron. Lett.*, Vol. 36, pp. 2034-2036.

Ito, H.; Furuta, T.; Kodama, S. & Ishibashi, T. (2000b). InP/InGaAs uni-travelling-carrier photodiode with a 310 GHz bandwidth, *Electron. Lett.*, Vol. 36, pp. 1809-1810.

Ito, H.; Furuta, T.; Kodama, S. & Ishibashi, T. (2000c). High-efficiency unitraveling-carrier photodiode with an integrated total-reflection mirror, *IEEE J. Lightwave Technol.*, Vol. 18, No. 3, pp. 384-387.

Ito, H.; Furuta, T.; Ito, T.; Muramoto, Y.; Tsuzuki, K.; Yoshino, K. & Ishibashi, T. (2002). W-band uni-travelling-carrier photodiode module for high-power photonic millimetre-wave generation, *Electron. Lett.*, Vol. 38, pp. 1376-1377.

Ito, H.; Nagatsuma, T.; Hirata, A.; Minotani, T.; Sasaki, A.; Hirota, Y. & Ishibashi, T. (2003a). High-power photonic millimetre-wave generation at 100 GHz using matching-circuit-integrated uni-travelling-carrier photodiodes, *IEE Proc. Optoelectron.*, Vol. 150, No. 2, pp. 138-142.

Ito, H.; Ito, T.; Muramoto, Y.; Furuta, T. & Ishibashi, T. (2003b). Rectangular waveguide output uni-traveling-carrier photodiode module for high-power photonic millimeter-wave generation in the F-band, *IEEE J. Lightwave Tech.*, Vol. 21, pp. 3456-3462.

Ito, H.; Kodama, S.; Muramoto, Y.; Furuta, T.; Nagatsuma, T. & Ishibashi, T. (2004a). High-speed and high-output InP/InGaAs uni-traveling-carrier photodiodes, *IEEE J. Selected Topics in Quantum Electronics*, Vol. 10, No. 4, pp. 709-727.

Ito, H.; Furuta, T.; Nakajima, F.; Ito, T.; Muramoto, Y. & Ishibashi, T. (2004b). Photonic generation of millimetre- and submillimetre-waves using rectangular-waveguide-output uni-travelling-carrier photodiode module, *Electron. Lett.*, Vol. 40, pp. 387-388.

Ito, H.; Furuta, T.; Kosugi, T.; Takahashi, H.; Hirata, A.; Muramoto, Y.; Tokumitsu, M.; Sato, Y.; Nagatsuma, T. & Ishibashi, T. (2005a). Over-10-dBm output uni-traveling-carrier photodiode module integrating a power amplifier for wireless transmission in the 125-GHz band," *IEICE Electron. Express*, Vol. 2, No. 16, pp. 446-450.

Ito, H.; Furuta, T.; Nakajima, F.; Yoshino, K. & Ishibashi, T. (2005b). Photonic generation of continuous THz wave using uni-traveling-carrier photodiode, *IEEE J. Lightwave Tech.*, Vol. 23, pp. 4016-4021.

Ito, H.; Furuta, T.; Muramoto, Y.; Ito, T. & Ishibashi, T. (2006). Photonic millimetre- and sub-millimetre-wave generation using the J-band rectangular-waveguide-output uni-travelling-carrier photodiode module, *Electron. Lett.*, Vol. 42, pp. 1424-1425.

Ito H. & Kodama, S. (2008). Uni-traveling-carrier photodiode (UTC-PD) and PD-EAM optical gate integrating a UTC-PD and a traveling wave electro-absorption modulator, In: *Ultrafast All-Optical Signal Processing Devices*, H. Ishikawa Ed., pp. 89-153, Wiley, West Sussex.

Ito, H.; Yoshino, K.; Muramoto, Y.; Yamamoto, H. & Ishibashi, T. (2010). Sub-terahertz-wave transceiver module integrating uni-traveling-carrier photodiode, Schottky barrier diode, and planar circulator circuit, *Proc. Int. Conf. on Infrared, Millimeter, and Terahertz Waves*, Tu-P.55.

Jun, D.-H.; Jang, J.-H.; Adesida, I. & Song, J.-I. (2006). Improved efficiency-bandwidth product of modified uni-traveling carrier photodiode structures using an undoped photo-absorption layer, *Jpn. J. Appl. Phys.*, vol. 45, No. 4B, pp. 3475-3478.

Kato, K.; Hata, S.; Kawano, K. & Kozen, A. (1993). Design of ultrawide-band, high-sensitivity p-i-n photodetectors, *IEICE Trans. Electron.*, Vol. E76-C, No. 2, pp. 214-221.

Kohjiro, S.; Kikuchi, K.; Maezawa, M.; Furuta, T.; Wakatsuki, A.; Ito, H.; Shimizu, N.; Nagatsuma, T. & Kado, Y. (2008). A 0.2-0.5 THz single-band heterodyne receiver based on a photonic local oscillator and a superconductor-insulator-superconductor mixer," *Appl. Phys. Lett.*, Vol. 93, 093508.

Kroemer, H. (1982). Heterostructure bipolar transistors and integrated circuits, *Proc. IEEE*, Vol. 70, No. 1, pp. 13-25.

Li, X.; Li, N.; Zheng, X.; Demiguel, S.; Campbell, J. C.; Tulchinsky, D. A. & Williams, K. J. (2003). High-saturation-current InP-InGaAs photodiode with partially depleted absorber, *IEEE Photonics Technol. Lett.*, Vol. 15, No.9, pp. 1276-1278.

Li, N.; Li, X.; Demiguel, S.; Zheng, X.; Campbell, J. C.; Tulchinsky, D. A.; Williams, K. J.; Isshiki, T. D.; Kinsey, G. S. & Sudharsansan, R. (2004). High-saturation-current

charge-compensated InGaAs-InP uni-traveling-carrier photodiode, *IEEE Photonics Technol. Lett.*, Vol. 16, No. 3, pp. 864-866.

Malcoci, A.; Stöhr, A.; Sauerwald, A.; Schulz, S. & Jäger, D. (2004). Waveguide and antenna coupled traveling-wave 1.55-μm photodetectors for optical (sub)millimeter-wave generation, *Proc. SPIE*, No. 5466, pp. 202-209.

Muramoto, Y.; Kato, K.; Mitsuhara, M.; Nakajima, O.; Matsuoka, Y.; Shimizu, N. & Ishibashi, T. (1998). High-output voltage, high speed, high efficiency uni-traveling-carrier waveguide photodiode," *Electron. Lett.*, Vol. 34, pp. 122-123.

Muramoto Y. & Ishibashi, T. (2003). InP/InGaAs pin photodiode structure maximizing bandwidth and efficiency, *Electron. Lett.*, Vol. 39, pp. 1749-1750.

Nagatsuma, T.; Song, H.-J.; Fujimoto, Y.; Miyake, K.; Hirata, A.; Ajito, K.; Wakatsuki, A.; Furuta, T.; Kukutsu, N. & Kado, Y. (2009a). Giga-bit wireless link using 300-400 GHz bands, *Tech. Dig. IEEE International Topical Meeting on Microwave Photonics*, Th.2.3.

Nagatsuma, T. ; Kumashiro, T.; Fujimoto, Y.; Taniguchi, K.; Ajito, K.; Kukutsu, N.; Furuta, T.; Wakatsuki, A & Kado, Y. (2009b). Millimeter-wave imaging using photonics-based noise source, *Proc. Int. Conf. on Infrared, Millimeter, and Terahertz Waves*, M3C05.0088 .

Nagatsuma, T.; Song H.-J. & Kado, Y. (2010a). Challenges for ultrahigh-speed wireless communications using terahertz waves," *Terahertz Science and Technology*, Vol.3, No.2, pp. 55-65.

Nagatsuma, T.; Kaino, A.; Hisatake, S.; Ajito, K.; Song, H.-J.; Wakatsuki, A.; Muramoto, Y.; Kukutsu, N. & Kado, Y. (2010b). Continuous-wave terahertz spectroscopy system based on photodiodes, *PIERS Online*, Vol. 6, No. 4, pp: 390-394.

Nakajima, F.; Furuta, T. & Ito, H. (2004). High-power continuous-terahertz-wave generation using a resonant-antenna-integrated uni-traveling-carrier photodiode," *Electron. Lett.*, Vol. 40, pp. 1297-1299.

Oh, K.-H.; Shimizu, N.; Kohjiro, S.; Kikuchi, K.; Wakatsuki, A.; Kukutsu, N. & Kado, Y. (2009). High-sweeping-speed optically synchronized dual-channel terahertz-signal generator for driving a superconducting tunneling mixer and its application to active gas sensing, *OPTICS EXPRESS*, Vol. 17, No. 21, pp. 18455-18461.

Redo-Sanchez, A.; Karpowicz, N.; Xu, J., & Zhang X.-C. (2006). Damage and defect inspection with terahertz waves", *Proc. 4th Intern. Workshop on Ultrasonic and Advanced Methods for Nondestructive Testing and Material Characterization*, pp. 67-77.

Rouvalis, E.; Renaud, C. C.; Moodie, D. G.; Robertson, M. J. & Seeds, A. J. (2010). Traveling-wave uni-traveling carrier photodiodes for continuous wave THz generation, *Optics Express*, Vol. 18, pp. 11105-11110.

Shi, J.-W.; Wu, Y.-S.; Wu, C.-Y.; Chiu, P.-H. & Hong, C.-C. (2005). High-speed, high-responsivity, and high-power performance of near-ballistic uni-traveling-carrier photodiode at 1.55-μm wavelength, *IEEE Photonics Technol. Lett.*, Vol. 17, No. 9, pp. 1929-1931.

Shimizu, N.; Watanabe, N.; Furuta, T. & Ishibashi, T. (1998). InP-InGaAs uni-traveling-carrier photodiode with improved 3-dB bandwidth of over 150 GHz, *IEEE Photonics Technol. Lett.*, Vol. 10, No. 3, pp. 412-414.

Song, H.-J.; Shimizu, N.; Furuta, T.; Suizu, K.; Ito, H. & Nagatsuma, T. (2008a). Broadband-frequency-tunable sub-terahertz wave generation using an optical comb signal,

AWGs, optical switches, and uni-travelling carrier photodiode for spectroscopic applications, *IEEE J. Lightwave Technol.*, Vol. 26, No. 15, pp. 2521-2530.

Song, H.-J.; Shimizu, N.; Furuta, T.; Wakatsuki, A. & Nagatsuma, T. (2008b). Subterahertz noise signal generation using a photodetector and wavelength-sliced optical noise signals for spectroscopic measurement, *Appl. Phys. Lett.*, Vol. 93, 241113.

Stöhr, A.; Malcoci, A.; Sauerwald, A.; Mayorga, I. C.; Güsten, R. & Jäger, D. S. (2003). Ultra-wide-band traveling-wave photodetectors for photonic local oscillators, *IEEE J. Lightwave Tech.*, Vol. 21, pp. 3062-3070.

Suzuki, H.; Fujiwara, M.; Iwatsuki, K.; Hirata, A. & Nagatsuma, T. (2005). Photonic millimetre-wave generator using intensity and phase modulators for 10 Gbit/s wireless link, *Electron. Lett.*, Vol. 41, No. 6, pp. 355-356.

Tebbenham R. L. & Walsh, D. (1975). Velocity/field characteristics of n-type indium phosphide at 110 and 330 K, *Electron. Lett.*, Vol. 11, pp. 96-97.

Wakatsuki, A.; Furuta, T.; Muramoto, Y.; Yoshimatsu, T. & Ito, H. (2008). High-power and broadband sub-terahertz wave generation using a J-band photomixer module with rectangular-waveguide output port, *Proc. Int. Conf. on Infrared, Millimeter, and Terahertz Waves*, pp. 1999-1-1999-2.

Williams, K. J.; Esman, R. D. & Dagenais, M. (1994). Effects of high space-charge fields on the response of microwave photodetectors, *IEEE Photonics Technol. Lett.*, Vol. 6, No. 5, pp. 639-641.
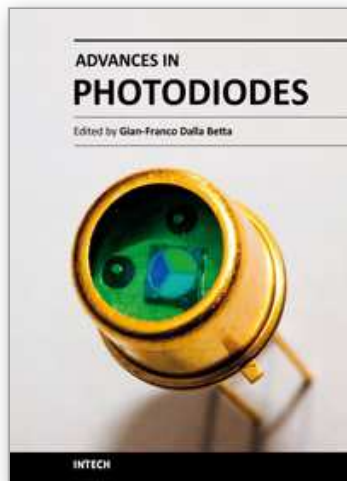
Advances in Photodiodes

Edited by Prof. Gian Franco Dalla Betta

Photodiodes, the simplest but most versatile optoelectronic devices, are currently used in a variety of applications, including vision systems, optical interconnects, optical storage systems, photometry, particle physics, medical imaging, etc. Advances in Photodiodes addresses the state-of-the-art, latest developments and new trends in the field, covering theoretical aspects, design and simulation issues, processing techniques, experimental results, and applications. Written by internationally renowned experts, with contributions from universities, research institutes and industries, the book is a valuable reference tool for students, scientists, engineers, and researchers.

How to reference

In order to correctly reference this scholarly work, feel free to copy and paste the following:

Tadao Nagatsuma and Hiroshi Ito (2011). High-Power RF Uni-Traveling-Carrier Photodiodes (UTC-PDs) and Their Applications, Advances in Photodiodes, Prof. Gian Franco Dalla Betta (Ed.), ISBN: 978-953-307-163-3, InTech, Available from: http://www.intechopen.com/books/advances-in-photodiodes/high-power-rf-uni-traveling-carrier-photodiodes-utc-pds-and-their-applications

INTECH
open science | open minds